Cyclic behaviour of 3D-woven composites in tension: Experimental testing and macroscale modelling

Composites: Part A 187 (2024) 108354

Contents lists available at ScienceDirect

Composites Part A

journal homepage: www.elsevier.com/locate/compositesa

Cyclic behaviour of 3D-woven composites in tension: Experimental testing and macroscale modelling

Carolyn Oddy [a,c,*], Meng yi Song [b], Christian Stewart [b], Bassam El Said [b], Magnus Ekh [a], Stephen R. Hallett [b], Martin Fagerström [a]

[a] Department of Industrial and Materials Science, Chalmers University of Technology, SE-412 96 Gothenburg, Sweden
[b] Bristol Composites Institute, University of Bristol, BS8 1TR Bristol, United Kingdom
[c] Department of Composites and Inspection, GKN Aerospace Sweden, 461 38 Trollhättan, Sweden

ARTICLE INFO

Keywords:
3D-woven composites
Cyclic loading
Local damage
Plasticity
Macroscale modelling

ABSTRACT

Composites with 3D-textile reinforcement present several engineering advantages. However, their intricate yarn architecture also creates a material with a number of nonlinear behaviours and features, which need to be understood in order to enable their efficient use. To demonstrate the anisotropic development of such non-linear behaviours, and how they depend on loading mode, tensile samples of a 3D-woven layer-to-layer angle interlock carbon-fibre reinforced epoxy composite are tested experimentally (data shared publicly). More specifically, specimens are cut and tested at orientations of 0°, 15°, 30°, 45° and 90° relative to the direction of the warp yarns. The samples are tested cyclically by loading and unloading them at progressively higher displacement values. By monitoring the reduction in stiffness and the development of permanent strains it is possible to identify material parameter values used to calibrate an anisotropic macroscale elasto-plastic damage model. The model shows promising agreement with the experimental results.

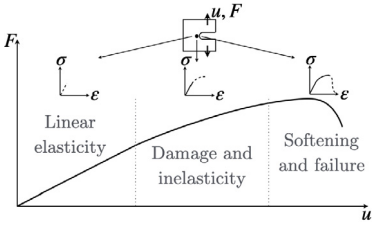

Fig. 1. A schematic for the three main regions of deformation behaviour exhibited by 3D-woven composites.

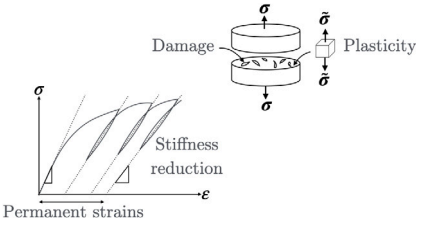

Fig. 2. A figure showing a sketch of the meaning of effective (undamaged) stress $\tilde{\sigma}$ in comparison to stress σ as well as a schematic showing how stiffness degradation and permanent strain development can be tracked in a cyclic test.

Analysis approaches for 3D-woven can generally be grouped into three categories. More specifically, those that consider the material on the microscale, the mesoscale and the macroscale. Out of these scales, the mesoscale, in which the yarns and polymer matrix are explicitly modelled, is the most widely analysed. To do so, a representative unit cell model of the impregnated yarn architecture is created first, which in itself is a challenging task, see for example Stig and Hallström [1] and Lomov et al. [2]. Most authors then turn to constitutive models which use standard continuum damage mechanics and inelastic constitutive models to describe the behaviour of the material constituents (impregnated yarns and matrix), see for example Green et al. [3], Lomov et al. [4], Topalidis et al. [5] and Mazumder et al. [6].

While subscale models allow for detailed descriptions and predictions of subscale features and failure mechanisms, they are computationally expensive. This makes analysing a full structural component infeasible. In order to improve computational efficiency others have turned to either multiscale approaches, c.f. Hirsekorn et al. [7] and Shah et al. [8]. Others, such as El Said et al. [9] subdivide the geometry

* Corresponding author at: Department of Industrial and Materials Science, Chalmers University of Technology, SE-412 96 Gothenburg, Sweden.
E-mail address: carolyn.oddy@chalmers.se (C. Oddy).

https://doi.org/10.1016/j.compositesa.2024.108354
Received 17 April 2024; Received in revised form 13 June 2024; Accepted 6 July 2024
Available online 16 July 2024

into different domains. In their approach highly loaded regions are modelled using a mesoscale approach while the remaining geometry is modelled on the macroscale. However, as discussed by Hurmane et al. [10], macroscale models are by far the most computationally efficient and industrially applicable. The Onera Damage Model for Polymer Matrix Composites [10], is an example of such a macroscale model which uses a combination of damage and viscoelastic constitutive models to predict how 3D-woven composites deform.

The primary focus of the current work is to conduct an experimental testing campaign to obtain a better understanding of what phenomena are causing the non-linearity in the second region, as illustrated in Fig. 1. The results are then used to calibrate and validate an anisotropic macroscale elasto-plastic damage model, see Oddy et al. [11]. Focus is given towards ensuring that the calibration parameters can be extracted directly from the experimental results without the need for complex calibration routines.

More specifically, the testing campaign involves loading and unloading the material cyclically at progressively higher strain levels. Similar methods have previously been applied to traditional laminated composites, e.g. Ladavèze et al. [12], Zscheyge et al. [13] as well as 3D-woven composites, e.g. Marcin [14]. It should, however, be noted at this time that the restriction has been made in this analysis to evaluating the material performance under only in-plane tensile and shear loads.

By cyclically loading the material in this way, it becomes possible to distinguish between two main non-linear mechanisms. As illustrated in Fig. 2, calculating the degradation of stiffness at each cycle, gives a strong indication and description of how damage is developing within the material. In a similar way, the permanent strain can be calculated at each loading cycle to give an indication of the mechanisms which cause permanent strain and hardening to develop. Further, in order to understand the anisotropic nature of this material, multiple loading orientations are considered. This includes tensile loading along the two nominal in-plane reinforcement directions as well as off-axis loading to induce different combinations of tensile and shear loading in the material oriented system. The experimental results are available in an open access repository, with more information found in the Appendix.

Following the experimental test campaign, attention is given to predicting the mechanical response of this material. As previously discussed, this work focuses primarily on analysing and capturing the material response in the first two regions illustrated in Fig. 1. This is carried out by building upon a phenomenologically based macroscale model developed by Oddy et al. [11]. The experimental test results obtained are used to calibrate and validate this anisotropic elastoplastic-damage model for 3D-woven composites. When formulating such a model, a choice must be made when it comes to how the damage and plasticity should interact. As discussed by Grassl and Jirásek [15], the two main options are defined by whether or not the plasticity model is formulated based on the damage or undamaged stress. The model considered here uses the latter option. As illustrated in Fig. 2 for a 1D problem, from a physical point view it means that the damaged material is subjected to a stress $\boldsymbol{\sigma}$. However, plasticity solely acts on the undamaged material which is subjected to a higher so called effective stress, $\tilde{\boldsymbol{\sigma}}$. The main advantage here is that this decouples the development of damage and plastic strain, which in turn simplifies parameter identification and model implementation.

It is noted here that predicting the material behaviour in the third region requires not only a very different experimental testing campaign, see for example Médeau et al. [16], but also different numerical techniques. In particular, when the constitutive material response must capture a load drop and softening, local damage models are no longer applicable as they lead to a loss of ellipticity of the governing equations, cf. Ottonsen and Ristinmaa [17]. To overcome this, a number of methods are possible and have been applied to 3D-woven composites. See for example Médeau [18]. These methods can include for example phase-field models, integral type non-local damage models or gradient enhanced damage models, cf. for example Miehe et al. [19], Pijaudier-Cabot and Bažant [20] and Peerlings et al. [21] respectively. For this reason, the third region is not considered in this analysis.

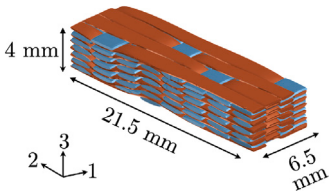

Fig. 3. Illustration of the material unit cell of the considered layer-to-layer angle interlock. Warp yarns are shown in blue while the weft yarns are shown in red.

1. Experimental test setup

1.1. Material description

The 3D-woven composite material considered here has a layer-to-layer angle interlock reinforcement. Layer-to-layer angle interlocks are characterised by the interlacing of warp and weft yarns in three dimensional space. More specifically, warp yarns are woven through multiple layers of weft yarns, providing out-of-plane reinforcement.

The considered layer-to-layer angle interlock is woven with yarns made from IM7 carbon fibres. The weave architecture is shown in Fig. 3 where the warp yarns, i.e. the main weaving direction, are shown in blue and made from HexTow IM7 24k tows. The weft yarns, made from HexTow IM7 12k tows, are shown in red. The particular weaving architecture of this material has a representative volume element (RVE) with an approximate size of 6.5 mm in the warp direction, 21.5 mm in the weft direction and 4 mm in the out-of-plane direction. This is also illustrated in Fig. 3, together with a 123 coordinate system that denotes the nominal warp, weft and thickness directions, respectively.

Specimens used for the experimental testing were manufactured using resin transfer moulding (RTM). The dry woven preforms, once trimmed, were approximately 500 mm long in the warp direction, 190 mm wide in the weft direction and 4 mm thick. The available flat panel RTM tool had width and length dimension of 500 × 500 mm, while the thickness was 4 mm. For this reason,when manufacturing each panel two preforms were placed next to each other in the tool. The additional space in the tool was filled using additional material with a similar permeability. In total, two panels (each containing two preforms) were infused using RTM6 epoxy [22]. The panels were initially cured in-tool for 3 h at 140 °C. This was followed by an oven post cure at 180 °C for 2.5 h.

1.2. Specimen orientation and dimensions

The woven substructure in 3D-woven composites results in a material that shows a high level of anisotropy. As previously discussed, this means that, to properly calibrate a representative macroscale model, data from experimental tests loaded in multiple directions is required. As this study is restricted to the tensile and shear in-plane properties, it means that at minimum, for calibration, the material needs to be tested in tension in the warp and weft reinforcement directions as well as in shear.

It should be emphasised, that the considered material has a relatively balanced weave, which was assumed to therefore produce relatively similar mechanical characteristics in the two main reinforcement directions. As a consequence, to quantify the shear behaviour, the approach considered here is to load 45° off-axis samples in tension. The balanced nature of the weave means that the specimens will experience a global uniaxial stress without any form of global lateral or shear stress or deformation. Note, however, in the case of a more unbalanced weave, the specimen will deform in an ‘s’ shape leading to non-uniform stress and strain distributions. As discussed by Tarnopol’skii and Kincis [23] however, this can be overcome by selecting a different, more

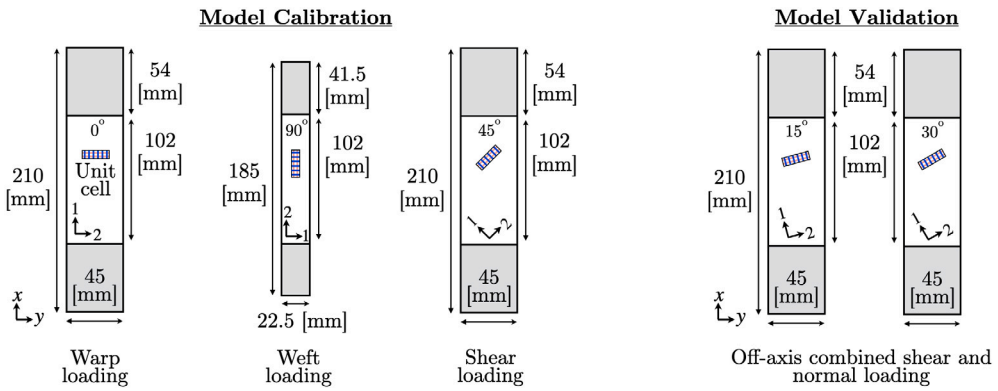

Fig. 4. Illustration of the different test specimens considered in this analysis. The images shows the dimension of the test specimen, unit cell and reinforcement orientation. Note again that 123 indicates the local material oriented coordinate system while xyz indicates the global system.

optimum, off-axis angle. It is also possible to modify the grips on the test machine, see for example Sun and Berreth [24].

In terms of testing carried out for model validation purposes, and to gain a greater understanding of how 3D-woven composites behave under mixed-mode loading, a number of off-axis orientations were also tested in tension. The different off-axis orientations induce different combinations of reinforcement oriented tensile and shear loads on the material. Due to limitations in the availability of 3D-woven preforms, and as the considered material is relatively balanced, the decision was made to focus on off-axis angles between 0° (i.e. samples aligned in the warp direction) and 45°. Specifically, additional off-axis angles of 15° and 30° were tested.

Selecting the dimensions of rectangular tensile specimens for 3D-woven composites is not necessarily a trivial task. There is a general lack of testing standards and a wide variation in the representative unit cell size between weave architectures. This is further complicated given that many weaves have large unit cell sizes. For this reason, it was decided that the 0° (warp aligned), 15°, 30° and 45° samples, would have a width of 45 mm (corresponding to two unit cells across the width for the 0° specimen) and a height of 210 mm. Limiting the width to two unit cells meant that it was sufficient to use a machine with a 250 kN load cell for the testing. Additionally, the chosen specimen length left a sufficient clamping length for the grips (minimum 60% for a grip depth of 90 mm to prevent pivoting), while still having a gauge region of 102 mm. This is illustrated in Fig. 4. A minimum of four samples for each orientation were cut from the panels.

The choice for sample width of the 90° (weft aligned) specimens is more challenging. As previously stated in Section 1.1, the woven preforms were relatively narrow in the weft direction (190 mm). Allowing margin for cutting, this means that the maximum length of the 90° samples was 185 mm. When accounting for sufficient grip distance this creates a sample with a short gauge region, especially when considering the unit cell length in the weft direction (21.5 mm). For this reason the decision was made to decrease the width of the weft-aligned samples to half of that of the other samples, i.e. 22.5 mm (approximately 3.5 times the unit cell width). This has two positive impacts. Firstly, by cutting the samples in half, they could be tested on a machine with a smaller load cell which also has a smaller grip. Secondly, as discussed by Adams et al. [25], for anisotropic materials, the length of the region where end effects from the grips influence the stresses is directly proportional to the width of the specimen. By decreasing specimen width, the area over which uniform stress is found in the gauge region increases. Specifically, a grip distance of 41.5 mm was used (75% for grip depth of 55 mm), leaving once again a gauge length of 102 mm. In this case it was possible to prepare eight test samples aligned in the weft direction. This is illustrated in Fig. 4.

1.3. Experimental procedure

The wider 0°, 15°, 30° and 45° samples were tested on an Instron 1342 test machine with a 250 kN load cell. The 90° specimens, however, were tested on an Instron 8801 test machine with a 100 kN load cell. In order to study the displacement and strain fields, a speckle pattern was sprayed on the test samples and a stereo digital image correlation (DIC) system was used.

The general goal was to have at least 5 equally spaced unloading cycles before the first significant load drop took place in each test. In order to best estimate at what cross-head displacement values to unload at, for each test specimen orientation, one sample was tested monotonically to failure. For each subsequent cyclic test, each cycle consisted of:

1. A displacement controlled loading period up to a predefined cross-head displacement value with a loading rate of 1.8 mm/min.
2. A force controlled unloading cycle to a load value of 5 kN. This ensured that the samples were not loaded in compression. The software required that the unloading rate be defined in N/min. As such, the initial monotonic test was used to estimate an unloading rate in N/min which corresponded to approximately 1.8 mm/min. Note that this meant the unloading rate expressed in N/min varied for each cycle.

In the following load–unloading cycles, the sample is progressively loaded to higher and higher cross-head displacements. For each test sample, during post processing, the displacement signal was extracted using a virtual extensometer in the DIC software Davis 10.1 [26] that was 100 mm in length.The images DIC images were all post-processed using a subset size of 33 pixels and a step size of 11 pixels.

2. Experimental results and discussion

2.1. Testing warp-aligned samples

A total of four samples, in which the warp yarns were aligned with the loading direction, were tested. Initially one specimen was tested monotonically with the goal of estimating appropriate displacement levels at which to unload the coming test specimens. The monotonic test specimen, however, showed the development of a non-representative strain concentration at the specimen edge, likely due to a small notch or imperfection. Shortly after this strain concentration was detected, a large crack was observed growing from this point. This lead to premature failure and the test was therefore deemed erroneous. The three remaining specimens were loaded and unloaded cyclically at progressively higher cross-head displacements. As the monotonic test could not be used to estimate suitable levels of deformation for

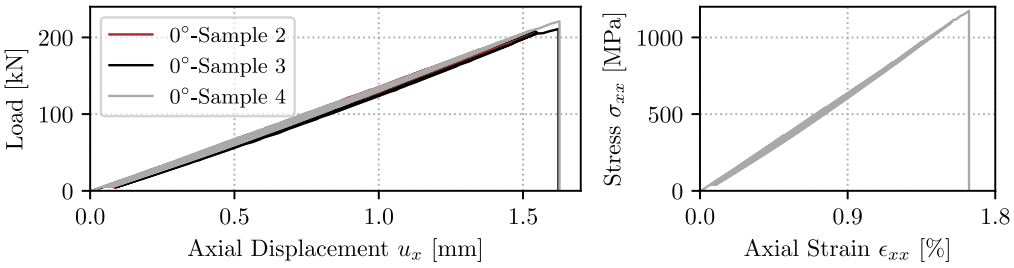

Fig. 5. Experimental test results of the warp-aligned samples. The load-displacement curves of the three test samples are show in the left image while the right image shows the stress-strain curve of Sample 4.

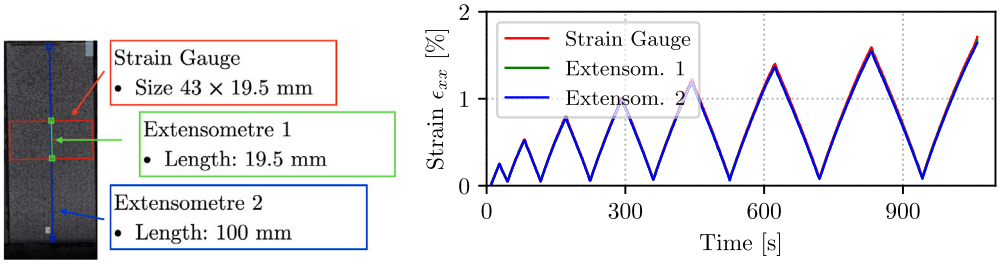

Fig. 6. Experimental test result comparison of the different axial strain measures for Sample 4 tested in the warp direction. The different extraction methods are illustrated in the image on the left while the image on the right shows the resulting strain-time curves.

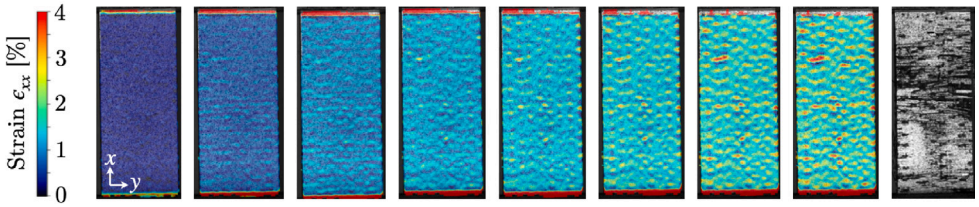

Fig. 7. DIC images showing axial strain distribution at the peak of each load cycle for Sample 4 tested in the warp direction.

progressive unloading, unloading displacements were instead estimated using simulation results from virtual testing of a mesoscale RVE of the same material, cf. Topalidis et al. [5]. The load–displacement results of these three samples are plotted in Fig. 5, and showed very consistent results.

Fig. 5 also shows the associated stress–strain curve for Sample 4. One thing to note initially, is that at each loading cycle the material stiffens slightly. This is likely due to the straightening of the reinforcement yarns. Note that in order to improve visualisation and aid in parameter extraction, discussed in Section 3.3, the resulting curve has been smoothed using a Butterworth filter [27]. It was however ensured that the peak and trough of each loading cycle was not disturbed.

The strain signal was extracted from the DIC software using three different measures, illustrated in Fig. 6. In all cases, it was ensured that the region over which the strain was measured included multiple unit cells. As can be seen in Fig. 6, regardless of whether a virtual strain gauge or virtual extensometer of different size was used, the resulting strain signal was very consistent. The overlapping curves are close to indistinguishable. Further, the axial strain distribution over the sample is shown in Fig. 7 at the peak of each loading cycle and following final failure. As can be seen, strain concentrations begin to form in the resin pockets uniformly over the sample, which then grow progressively in intensity as the test advances. Eventually the specimen undergoes a brittle and abrupt final failure as the warp yarns rupture at an axial strain of approximately 1.7%.

2.2. Testing weft-aligned samples

Once again, with the aim of being able to estimate appropriate displacements at which to unload the cyclically tested samples, a monotonic test was initially performed on a 90° specimen. The monotonic sample however showed signs of slippage, as well as cracking underneath the grips and was therefore deemed invalid. After adjusting the grip pressure, three samples were successfully tested under cyclic loading. The load displacement curves for each are plotted in Fig. 8 and show a high level of consistency.

The stress–strain curve associated with Sample 4 is also shown in Fig. 8. Again, different axial strain measures were extracted and analysed over regions large enough to contain multiple unit cells. The results, for Sample 4, are given in Fig. 9 and show that the axial strain signal is relatively unaffected regardless of whether it is averaged using a virtual strain gauge or extensometer. Failure took place at an axial strain level of approximately 1.7% and showed a brittle failure response governed by the rupturing of the weft yarns.

One factor to consider when analysing the DIC images, is that the narrower weft direction specimens, lead to highly apparent edge effects. Cracking and splintering can be clearly seen in Fig. 10, where once again the axial strain contours are shown and the images are taken at the top of each loading cycle. Therefore, the use of wider test samples should be further explored, and a balance found between having a sufficient gauge length relative to width.

2.3. Testing 45° off-axis samples

In order to quantify the behaviour of the material when loaded in shear, 45° off-axis tests were carried out. Unlike when the material is loaded along its reinforcements, this shear loading mode exhibits far greater apparent ductility, as seen in Fig. 11. In this case, Sample 1 was successfully loaded monotonically, while Sample 2, 3 and 4

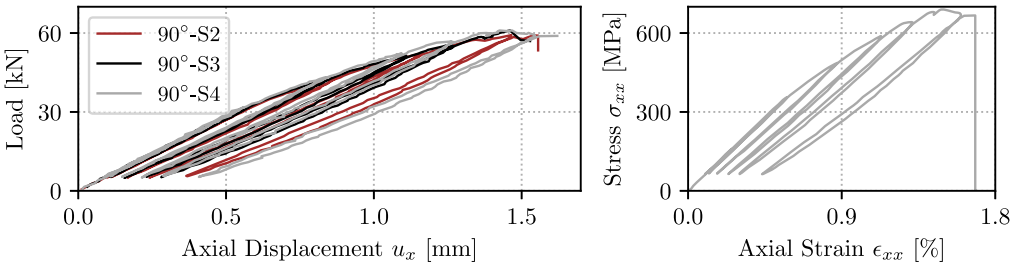

Fig. 8. Experimental test results of the weft-aligned samples. The load–displacement cures of the three test samples are shown in the image on the left while the image on the right shows the stress–strain curve of Sample 4.

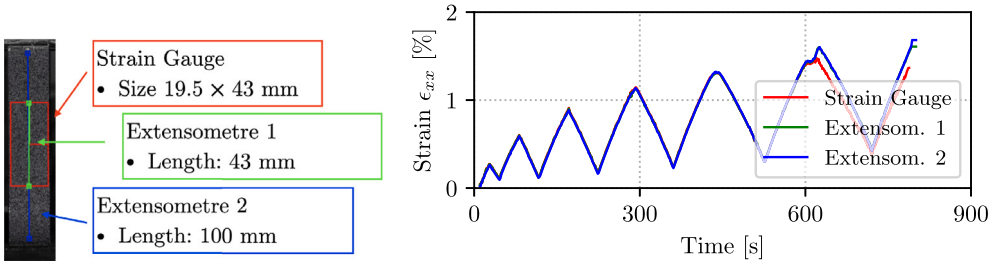

Fig. 9. Experimental test result comparison of the different axial strain measures for Sample 4 tested in the weft direction. The different extraction methods are illustrated in the image on the left while on the right the resulting strain-time curves are shown.

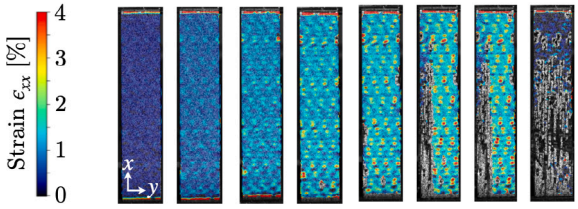

Fig. 10. DIC images showing the axial strain distribution at the peak of each load cycle for Sample 4 tested in the weft direction.

were loaded cyclically. It should also be noted, that while the load–displacement curves end at approximately 15 mm for Sample 3 and at 25 mm for the remaining samples, this is not because the specimens were no longer able to carry load. The DIC speckle pattern simply became so obstructed that a displacement signal could no longer be extracted. This can more clearly be seen in Fig. 12, in which the axial strain distribution is shown at the top of each loading cycle.

It is also apparent that after the initial load drop, the material begins to show prominent necking. This is accompanied by a realignment of the yarns towards the loading direction, stiffening of the material response and even pronounced out-of-plane expansion. Fig. 13 shows two images of Sample 2 taken after the test was completed, in which the yarn realignment and out-of-plane expansion are clearly visible.

The shear stress–strain response was extracted from the test as

$$\sigma_{12} = \frac{1}{2}\sigma_{xx} \text{ and } \gamma_{12} = \epsilon_{yy} - \epsilon_{xx}, \tag{1}$$

where the axial and transverse strain signals were extracted using the strain gauge of equivalent size and placement as that shown in red in Fig. 6. The extracted strain signals for Sample 2 are illustrated in Fig. 14 along with the material oriented shear stress–strain response. Note again, that at a shear strain value of approximately 35%, the speckle pattern is no longer sufficiently intact to be able to extract an accurate measurement. However, this takes place well after the load drop, and well after a small strain assumption is no longer valid. It is therefore not a hindrance to extracting the plasticity and damage behaviour for the shear loading mode.

2.4. Testing 15° off-axis samples

Loading off-axis tensile specimens at 15° induces a combination of both tensile and shear loading onto the material. Fig. 15 shows the load–displacement curves obtained by testing four different samples. The first sample was loaded monotonically to failure, while the remaining three were loaded cyclically.

Fig. 16 shows a contour plot of the axial strain development of Sample 4. The first eleven images are taken at the top of each loading cycle. One additional image is also shown in order for the failure behaviour to be better visualised. However it should be noted that in the case of Sample 4, at an axial displacement of approximately 7 mm, the speckle pattern was no longer sufficiently intact to extract a displacement signal. The test however did continue to progress, with the material showing increased softening until a load of 19 kN was reached and final failure took place.

It is clear that the deformation behaviour combines aspects seen in both the 0° and 45° off-axis tests. Following the peak load of approximately 70 kN, a shear band forms which is aligned along the direction of the warp yarns. The shear band grows and the specimen's deformation begins to clearly show an 'S' shape due to the combined multiaxial loading. Eventually, for all specimens, failure took place when the warp yarns ruptured. In the case of Sample 4, this can be seen adjacent to the lower grip.

2.5. Testing 30° off-axis samples

Testing the material at a 30° angle to the warp yarns also induces a combination of reinforcement aligned tensile and shear loading. In

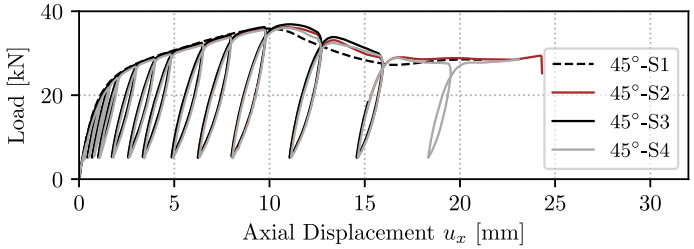

Fig. 11. Load–displacement curves of the four test samples tested at 45° off-axis. Sample 1 was tested monotonically, while the remaining three were tested cyclically.

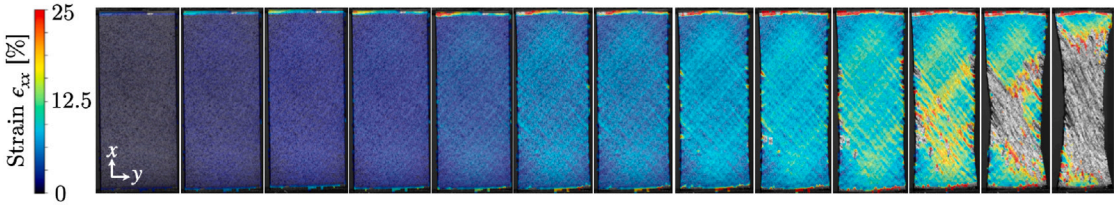

Fig. 12. DIC images showing axial strain distribution in the 45° off-axis test for Sample 2 at the peak of each load cycle.

Fig. 13. Images of Sample 2 (45° off-axis loading) taken after the test showing necking, realignment of yarns and out-of-plane expansion.

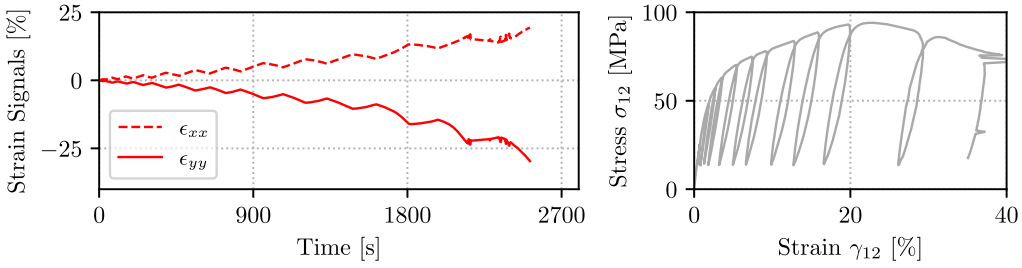

Fig. 14. Experimental test results of 45° off-axis test for Sample 2. Strain-time curves of the axial and transverse strain are shown in the figure on the left. They have been extracted from a 43 × 19.5 mm strain gauge located centrally in the gauge region. The shear stress–strain curve of Sample 2 is plotted in is plotted in the figure on the right.

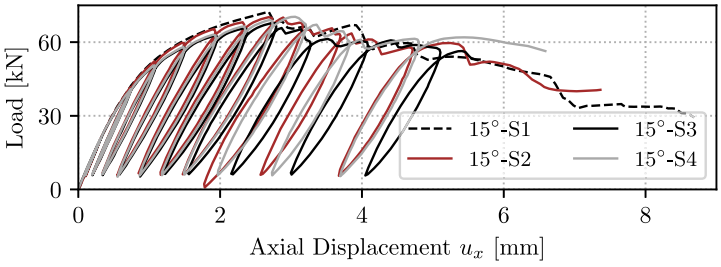

Fig. 15. Load–displacement curves of the four 15° off-axis test samples. Sample 1 was tested monotonically while the remaining three were tested cyclically.

Fig. 17, the load displacement curves for four, 30° off-axis samples are plotted. Again, the first sample was tested monotonically and used to estimate the appropriate timing of the load cycles for the remaining three. Fig. 18 shows the axial strain contours at the peak of each of the thirteen loading cycles as well as one image taken at after final failure for Sample 2.

The 30° angle induces greater levels of shear loading in the material, compared to those experienced by the 15° off-axis samples. The effects are clearly visible in the results. There is an initial load drop, followed by a region of softening before stiffening once again. A shear band forms, which is well aligned with the warp yarns. Unlike the 45° off-axis samples however, final failure of the sample did eventually take place with rupturing of the warp yarns, which ended the test. The curves in Fig. 17, all end once the DIC software was no longer able to extract a displacement signal. However, on average, the samples were able to continue to stiffen, reaching a load of approximately 38 kN.

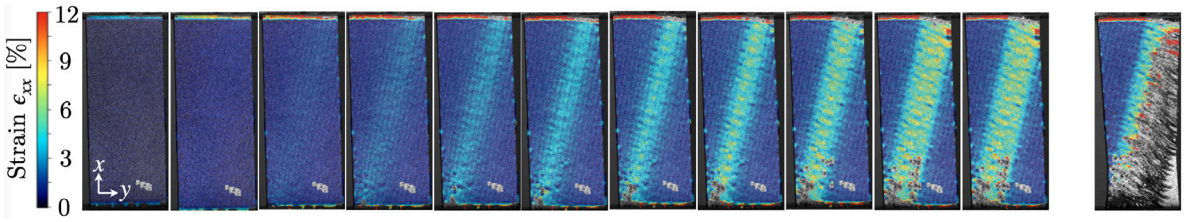

Fig. 16. DIC images showing the axial strain distribution in a 15° off-axis test sample at the peak of each load cycle and one taken at final failure for Sample 4.

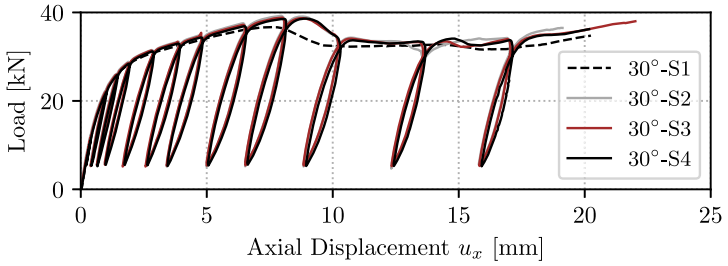

Fig. 17. Load–displacement curves of the four 30° off-axis test samples. Sample 1 was tested monotonically while the remaining three were tested cyclically.

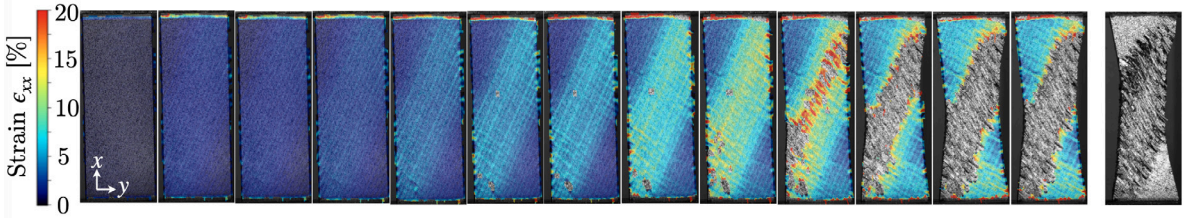

Fig. 18. DIC images showing the axial strain distribution in a 30° off-axis test sample at the peak of each load cycle and one taken at final failure for Sample 2.

3. Macroscale model description and extraction of calibration data

3.1. Model description

As previously discussed, the macroscale model adopted in this work relies on the assumption that the non-linear behaviour (before failure initiation) is due to a combination of stiffness degrading (i.e. damage) and permanent strain developing (i.e. plasticity) mechanisms on the subscales. Full details of the model formulation, thermodynamic considerations, implementation methods in commercial or in-house FE software as well as additional information can be found in Oddy et al. [11] and Oddy [28].

The considered macroscale model also assumes that the material can be considered orthotropic. Previous analyses have been carried out on a mesoscale FE-model of the considered yarn architecture, see Oddy et al. [29]. These analyses indicated that the resulting homogenised stiffness tensor is well described using orthotropy. This means that nine elastic material properties are required. Table 1 summarises the elastic properties for the considered material. The in-plane properties have been extracted from the experimental tests summarised in Section 2. As no out-of-plane testing has been conducted, the out-of-plane properties have been estimated using a mesoscale analysis. An FE model of an RVE of the material was developed in Topalidis et al. [5]. By loading the RVE in six unique loading modes, the complete stiffness tensor can be resolved, and the elastic properties computed. As shown in Oddy [28], the RVE analysis produced comparable in-plane elastic properties as those found experimentally.

To describe damage evolution, the model uses four damage variables (d_1, d_2, d_3 and d_s), each governing how the stiffness reduces under different loading modes. The first, d_1, represents damage associated with loading along the warp yarns. Likewise, d_2, represents damage associated with loading along the weft yarns, while d_3 denotes damage associated with out-of-plane loading. Finally, d_s describes damage development under shear loading. Then, adopting the standard assumption that the strain can be additively decomposed into an elastic and plastic component, i.e. $\boldsymbol{\epsilon} = \boldsymbol{\epsilon}_{el} + \boldsymbol{\epsilon}_p$, the constitutive stress–strain relation is given by

$$\boldsymbol{\sigma} = \underbrace{\left(1-d_s\right)\mathbb{E}_m : \left(\boldsymbol{e}-\boldsymbol{e}_p\right)}_{\text{shear}} + \underbrace{\left(1-d_1\right)\mathbb{E}_{f1} : \left(\boldsymbol{\epsilon}-\boldsymbol{\epsilon}_p\right)}_{\text{warp}} + \underbrace{\left(1-d_2\right)\mathbb{E}_{f2} : \left(\boldsymbol{\epsilon}-\boldsymbol{\epsilon}_p\right)}_{\text{weft}} + \underbrace{\left(1-d_3\right)\mathbb{E}_{f3} : \left(\boldsymbol{\epsilon}-\boldsymbol{\epsilon}_p\right)}_{\text{out-of-plane}}. \tag{2}$$

As indicated, this means that each term largely governs the warp, weft, out-of-plane or shear behaviour of the material. It is also important to note that $\boldsymbol{e}$ denotes the shear strains aligned in the 123-coordinate system.

In Oddy et al. [11] and Oddy [28], the full expressions for the stiffness tensors $\mathbb{E}_m$, $\mathbb{E}_{f1}$, $\mathbb{E}_{f2}$ and $\mathbb{E}_{f3}$ are derived from the use of structural tensors. This provides a convenient method to express the stiffness and material behaviours in a global xyz-coordinate system, to which the local (material-aligned) 123-coordinate system is not necessarily aligned. However, for ease of use and to help in visualisation, the

Table 1
Elastic parameters for the considered material. In plane properties have been extracted from the experimental results while the out-of-plane properties have been estimated using a mesoscale RVE analysis.

Stiffness [GPa]	E_1	70	E_2	63	E_3	10
Shear stiffness [GPa]	G_{12}	3.6	G_{13}	3.2	G_{23}	3.7
Poisson's ratio [-]	ν_{12}	0.06	ν_{13}	0.38	ν_{23}	0.46

components in Eq. (2) can be expressed in Voigt form. Using the elastic material properties given in Table 1, and the case where the 123-axis are aligned with the global xyz-axis system gives

$$\begin{aligned}\boldsymbol{\sigma} &= \begin{bmatrix}\sigma_{xx} & \sigma_{yy} & \sigma_{zz} & \sigma_{xy} & \sigma_{yz} & \sigma_{xz}\end{bmatrix}^{\mathrm{T}},\\ \boldsymbol{\epsilon} &= \begin{bmatrix}\epsilon_{xx} & \epsilon_{yy} & \epsilon_{zz} & \gamma_{xy} & \gamma_{yz} & \gamma_{xz}\end{bmatrix}^{\mathrm{T}}\\ \text{and}\quad \boldsymbol{e} &= \begin{bmatrix}0 & 0 & 0 & \gamma_{xy} & \gamma_{yz} & \gamma_{xz}\end{bmatrix}^{\mathrm{T}}.\end{aligned} \tag{3}$$

Further, the components of the stiffness tensor in Voigt form are then

$$\mathbb{E}_m = \begin{bmatrix}6.2 & 0 & 0 & 0 & 0 & 0\\ 0 & 8.2 & 0 & 0 & 0 & 0\\ 0 & 0 & 6.6 & 0 & 0 & 0\\ 0 & 0 & 0 & 3.6 & 0 & 0\\ 0 & 0 & 0 & 0 & 3.7 & 0\\ 0 & 0 & 0 & 0 & 0 & 3.2\end{bmatrix}\ [\text{GPa}],$$

$$\mathbb{E}_{f1} = \begin{bmatrix}72.7 & 2.94 & 2.57 & 0 & 0 & 0\\ 2.94 & 0 & 0 & 0 & 0 & 0\\ 2.57 & 0 & 0 & 0 & 0 & 0\\ 0 & 0 & 0 & 0 & 0 & 0\\ 0 & 0 & 0 & 0 & 0 & 0\\ 0 & 0 & 0 & 0 & 0 & 0\end{bmatrix}\ [\text{GPa}], \tag{4}$$

$$\mathbb{E}_{f2} = \begin{bmatrix}0 & 2.94 & 0 & 0 & 0 & 0\\ 2.94 & 64.95 & 2.15 & 0 & 0 & 0\\ 0 & 2.15 & 0 & 0 & 0 & 0\\ 0 & 0 & 0 & 0 & 0 & 0\\ 0 & 0 & 0 & 0 & 0 & 0\\ 0 & 0 & 0 & 0 & 0 & 0\end{bmatrix}\ [\text{GPa}],$$

$$\text{and } \mathbb{E}_{f3} = \begin{bmatrix}0 & 0 & 2.57 & 0 & 0 & 0\\ 0 & 0 & 2.15 & 0 & 0 & 0\\ 2.57 & 2.15 & 10.6 & 0 & 0 & 0\\ 0 & 0 & 0 & 0 & 0 & 0\\ 0 & 0 & 0 & 0 & 0 & 0\\ 0 & 0 & 0 & 0 & 0 & 0\end{bmatrix}\ [\text{GPa}]. \tag{5}$$

Note that this means, that if damage and plasticity do not develop or are not considered, Eq. (2) simplifies to $\boldsymbol{\sigma} = \mathbb{E} : \boldsymbol{\epsilon}$, where $\mathbb{E}$ is the orthotropic elastic stiffness tensor of the material.

What remains is to define how the damage and permanent strains development is governed in the macroscale model. This is done using standard yield and damage surfaces, see e.g. Simo and Hughes [30]. Considering first the plasticity model, the development of plastic strain is controlled by four yield surfaces with isotropic hardening, denoted ϕ_{p1}, ϕ_{p2}, ϕ_{p3} and ϕ_{ps}. As their names suggest, they each govern the development of plasticity in the warp direction, weft direction, out-of-plane direction and in shear respectively. Again, considering the case where the 123-material axes are aligned with the global xyz-system, these yield surfaces are expressed in terms of the effective stress (denoted with a $\tilde{\bullet}$) where

$$\phi_{p1} = \left|\tilde{\sigma}_{xx}\right| - \sigma_{y1} - \kappa_1\left(\boldsymbol{\epsilon_p}\right) \le 0, \quad \phi_{p2} = \left|\tilde{\sigma}_{yy}\right| - \sigma_{y2} - \kappa_2\left(\boldsymbol{\epsilon_p}\right) \le 0, \tag{6}$$

$$\phi_{p3} = \left|\tilde{\sigma}_{zz}\right| - \sigma_{y3} - \kappa_3\left(\boldsymbol{\epsilon_p}\right) \le 0$$
$$\text{and } \phi_{ps} = \sqrt{\tilde{\sigma}_{xy}^2 + \tilde{\sigma}_{yz}^2 + \tilde{\sigma}_{xz}^2} - \tau_y - \kappa_s\left(\boldsymbol{\epsilon_p}\right) \le 0. \tag{7}$$

In order to fully calibrate the plasticity model, it is necessary to determine the yield stresses that govern each loading mode σ_{y1}, σ_{y2}, σ_{y3}, τ_y. It is also necessary to propose expressions for how the isotropic hardening stress should develop in each loading mode, i.e. κ_1, κ_2, κ_3, κ_s, as a function of the plastic strain development.

The traditional implementation of a standard plasticity model makes use of what are referred to as *internal hardening variables* or *equivalent plastic strains*, denoted here by k. They act as scalar measures of the plastic strain tensor and are governed by the use of flow rules. However, in the case of the macroscale model described here, the flow rules are formulated such that the internal hardening variables are directly proportional to the plastic strain development in each reinforcement direction and in shear. So for ease and simplicity, they will not be introduced here. However, when it comes to model implementation, they must be considered.

Similarly, four damage surfaces are used to control how damage develops under loading in the warp direction, weft direction, out-of-plane direction and in shear. These are denoted ϕ_{d1}, ϕ_{d2}, ϕ_{d3} and ϕ_{ds} respectively. Before these can be stated, it is necessary to introduce their associated damage driving forces. These are formulated through thermodynamic argumentation, and for the considered model they are functions of strictly the elastic strain. For each respective loading mode, the damage driving forces are given by

$$\begin{aligned}Y_1 &= \frac{1}{2}\boldsymbol{\epsilon}_{el} : \mathbb{E}_{f1} : \boldsymbol{\epsilon}_{el}, \quad Y_2 = \frac{1}{2}\boldsymbol{\epsilon}_{el} : \mathbb{E}_{f2} : \boldsymbol{\epsilon}_{el},\\ Y_3 &= \frac{1}{2}\boldsymbol{\epsilon}_{el} : \mathbb{E}_{f3} : \boldsymbol{\epsilon}_{el} \text{ and } Y_s = \frac{1}{2}\boldsymbol{e}_{el} : \mathbb{E}_m : \boldsymbol{e}_{el}.\end{aligned} \tag{8}$$

Then, each damage surface consists of two parts: the damage driving force and a function, denoted η, to control how the damage should develop under each loading mode respectively. Specifically,

$$\phi_{d1} = Y_1 - \eta_1(d_1) \le 0, \quad \phi_{d2} = Y_2 - \eta_2(d_2) \le 0, \tag{9}$$

$$\phi_{d3} = Y_3 - \eta_3(d_3) \le 0 \text{ and } \phi_{ds} = Y_s - \eta_s(d_s) \le 0. \tag{10}$$

To summarise; under each loading mode, a calibration method must be used to determine the values of the yield stresses (σ_{y1}, σ_{y2}, σ_{y3}, τ_y) as well as appropriate expressions to control how the isotropic hardening stresses (κ_1, κ_2, κ_3, κ_s) should develop and how the damage development (η_1, η_2, η_3, η_s) should be controlled.

3.2. Extracting calibration data

The key to this calibration method is the assumption that for each uniaxial loading mode (tension along the warp, weft and out-of-plane directions as well as in shear), the constitutive equation given by Eq. (2) reduces down to a 1D case where $\sigma = (1-d)E\epsilon_{el}$. In turn, the development of damage and plasticity can be explored independently for each loading mode.

Considering a generic 1D constitutive response, what then needs to be determined is the yield stress, an expression for the isotropic hardening $\kappa(\epsilon_p)$ and an expression controlling the damage development $\eta(d)$. This can be done with relative ease by following the procedure outlined in Fig. 19. In more details, this requires

1. Decide where damage and plasticity should initiate. This can be at different locations and is a somewhat delicate choice. The simplest option is to choose a point visually based on where the curve begins to show a sufficiently non-linear response. From this, it is then possible to determine the yield stress σ_y, the initial elastic stiffness $E_{(0)}$, and the driving force at damage onset $Y_{(0)} = 1/2E_{(0)}\epsilon_{el(0)}^2$. Note here that the subscripts indicate the loading cycle number.
2. At the first unloading cycle, extrapolate the unloading curve to the strain axis, and determine the plastic strain $\epsilon_{p(1)}$ as well as the stiffness $E_{(1)}$.
3. From the plastic strain compute the elastic strain $\epsilon_{el(1)} = \epsilon_{(1)} - \epsilon_{p(1)}$, and from that the damage driving force $Y_{(1)} = 1/2E_{(0)}\epsilon_{el(1)}^2$. Then compute the damage $d_{(1)} = 1 - E_{(1)}/E_{(0)}$ and plot the damage and driving force at the first unloading cycle.
4. Compute the effective stress at the first unloading cycle $\tilde{\sigma}_{(1)} = \sigma_{(1)}/(1-d_{(1)})$, followed by the isotropic hardening stress $\kappa_{(1)} = \tilde{\sigma}_{(1)} - \sigma_y$. Plot the hardening stress against the plastic strain.

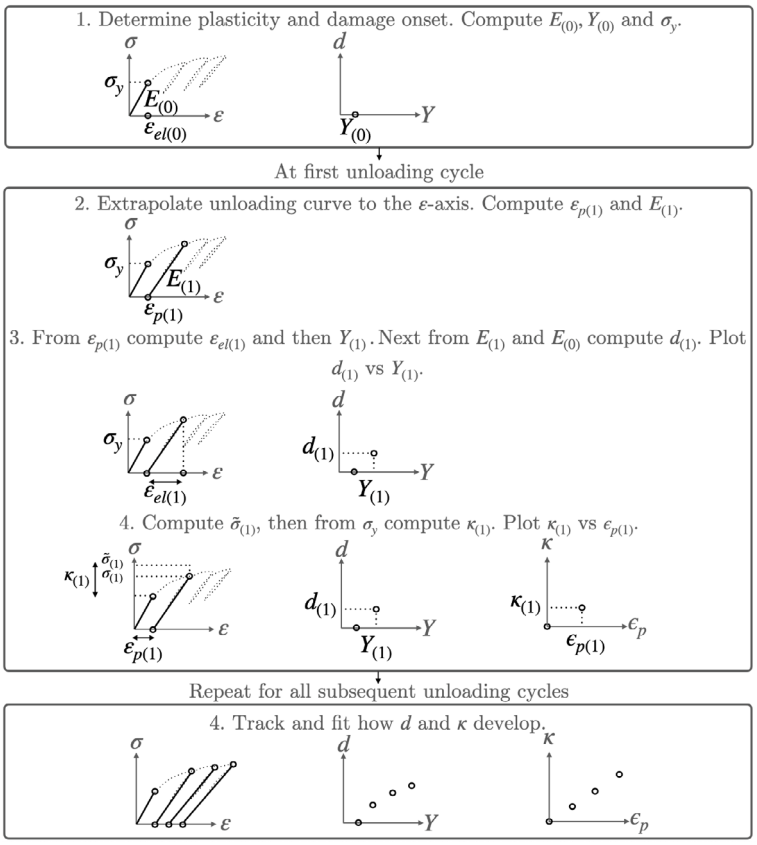

Fig. 19. A flow chart indicating the proposed calibration procedure for extracting damage and plasticity parameters from a uniaxial tensile cyclic test.

5. Repeat for all following loading cycles and propose a function to describe each 1D relationship.

After completing steps 1 through 5 for each uni-axial loading mode, a clear description can be seen of how damage and plasticity should develop in each loading mode. While theoretically, any expression for $\kappa(\epsilon_p)$ and $d(Y)$ can be chosen, one which is usually convenient and appropriate to use, is an exponential curve with saturation. In the case of the $\kappa - \epsilon_p$ relationship, this would correspond to $\kappa(\epsilon_p) = \kappa_{sat}\left(1 - e^{-c\epsilon_p}\right)$, where κ_{sat} defines the saturation value of the curve and the parameter c controls how steeply the curve approaches the saturation value. Note also that as the isotropic hardening stress should not begin to develop until plastic strain also begins developing. As such, this curve must also pass through the origin.

On the other hand, it is possible to delay the onset of damage development until a certain elastic strain (i.e. damage driving force) is reached. In that case, an onset value Y_o can be introduced into the curve definition meaning that it can be expressed as $d(Y) = d_{sat}\left(1 - e^{-b(Y-Y_o)}\right)$. Again, b controls how quickly the damage curve approaches its saturation value d_{sat}. The expression for $\eta(d)$ given in the yield surfaces, can then be determined by inverting the damage expression, i.e. in this case $\eta(d) = Y - \left(\frac{-\ln(1-d/d_{sat})}{b} + Y_o\right)$.

3.3. Calibration results

As previously discussed, the experimental test campaign focused solely on the in-plane behaviour of the considered 3D-woven composite. The calibration routine outlined in Fig. 19 was therefore carried out on one of the resulting stress–strain curves of the uniaxial tests carried out in the warp, weft and 45° directions.

Fig. 20 shows the results for cyclic loading in tension along the warp direction. One of the most striking details of this test, is the clear stiffening that the results show at each unloading, up to approximately 6%. This manifests itself as a 'negative' damage growth, likely due to yarns straightening as load is applied. While this stiffening effect should therefore perhaps not be referred to as 'damage', like damage, it leads to non-linear effects caused by a change in stiffness. It can therefore be numerically modelled using exactly the same traditional continuum damage mechanics tactics. Both the damage and permanent strain development showed a trend which could be well captured using an exponential function with saturation. This is illustrated in Fig. 20, while the relevant parameters for the curve fits are summarised in Tables 2 and 3.

When analysing the results of the weft aligned test sample, shown in Fig. 21, it is clear that there is a progressive increase in damage corresponding to a value of approximately 12% stiffness loss. This has been fit with an exponential curve with saturation, the parameters of which are summarised in Table 3. Note that the last unloading cycle took place after the load drop and while indicated in the damage-driving force and hardening stress-plastic strain plots, it was not considered when calibrating the parameters. Again, when considering the plastic strain — hardening stress development, the trend was fit using an exponential curve with saturation. The associated parameters are summarised in Table 2.

Finally, Fig. 22, shows the calibration routine carried out on the shear stress–strain curve extracted from the 45° off-axis test. The stress–strain curve was only considered up to the load drop. Once again, the development of damage and plasticity can be well captured using exponential curves with saturation. The associated parameters for each curve are summarised in Tables 2 and 3 respectively.

4. Macroscale modelling results and discussion

In order to demonstrate and evaluate the predictive capacity of the model, representative finite element models of the gauge region for each sample orientation were created. The nominal dimensions of each

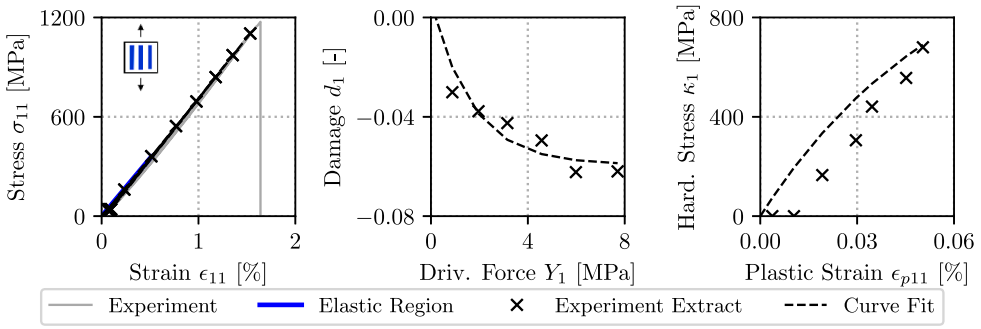

Fig. 20. Carrying out the calibration routine outlined in Fig. 19, on the cyclic uniaxial stress–strain curve shown in Fig. 5 when the material is loaded in the warp direction.

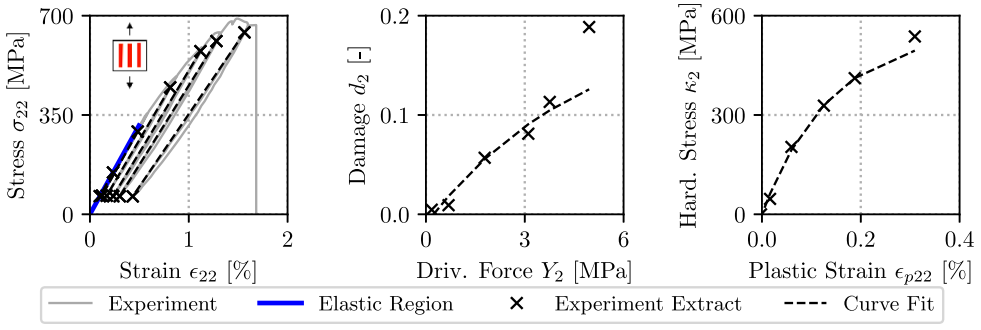

Fig. 21. Carrying out the calibration routine outlined in Fig. 19, on the cyclic uniaxial stress–strain curve shown in Fig. 8 when the material is loaded in the weft direction.

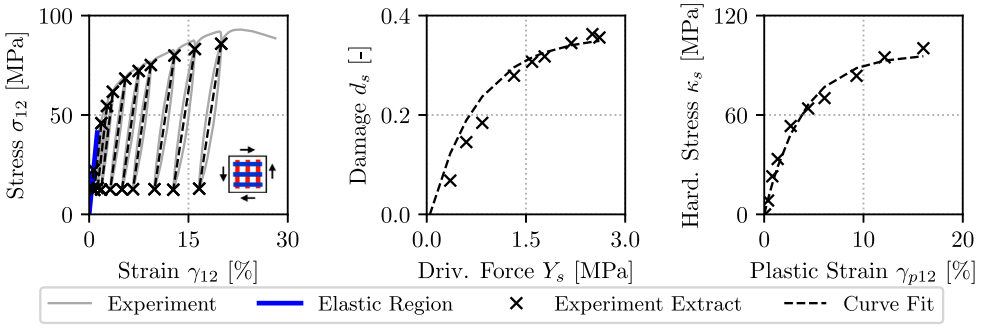

Fig. 22. Carrying out the calibration routine outlined in Fig. 19, on the cyclic uniaxial stress–strain curve shown in Fig. 14 when the material is loaded in shear.

Table 2
The plasticity model parameters.

Direction	Hardening law	Parameters
Warp	$\kappa_1 = \kappa_{sat,1}\left(1 - e^{-c_1\epsilon_{p11}}\right)$	$\kappa_{sat,1} = 1200$ [MPa], $\sigma_{y1} = 358$ [MPa], $c_1 = 1700$ [-]
Horizontal weft	$\kappa_2 = \kappa_{sat,2}\left(1 - e^{-c_2\epsilon_{p22}}\right)$	$\kappa_{sat,2} = 553$ [MPa], $\sigma_{y2} = 313$ [MPa], $c_2 = 725$ [-]
Shear	$\kappa_s = \kappa_{sat,s}\left(1 - e^{-c_s\gamma_{p12}}\right)$	$\kappa_{sat,s} = 96$ [MPa], $\tau_y = 42.5$ [MPa], $c_s = 25.9$ [-]

Table 3
The damage model parameters.

Direction	Damage variable	Parameters
Warp	$d_1 = d_{sat,1}\left(1 - e^{-b_1(Y_1 - Y_{o1})}\right)$	$Y_{o1} = 0.19$ [MPa], $b_1 = 0.59$ [1/MPa], $d_{sat,1} = -0.06$ [-]
Horizontal weft	$d_2 = d_{sat,2}\left(1 - e^{-b_2(Y_2 - Y_{o2})}\right)$	$Y_{o2} = 0.23$ [MPa], $b_2 = 0.21$ [1/MPa], $d_{sat,2} = 0.20$ [-]
Shear	$d_s = d_{sat,s}\left(1 - e^{-b_s(Y_s - Y_{os})}\right)$	$Y_{os} = 0.05$ [MPa], $b_s = 1.37$ [1/MPa], $d_{sat,s} = 0.37$ [-]

model correspond to those outlined in Fig. 4. More specifically, a three-dimensional FE-model of each gauge region was built in *ABAQUS* using fully integrated 3DC8 elements. The element size was selected to be sufficiently small such that the results showed mesh convergence.

In terms of selecting boundary conditions, it was important to take into account the compliance seen in the grips. The 0°, 90° and 45° test samples all showed more or less strictly vertical displacement at the boundaries. On the other hand, the anisotropy and misaligned nature of the 15° and 30° samples meant that they favoured an s-shaped deformation mode, leading to lateral displacement at both the upper and lower grip. For this reason, using the DIC-analysis the displacement was extracted at a central location at the edge of both the upper and

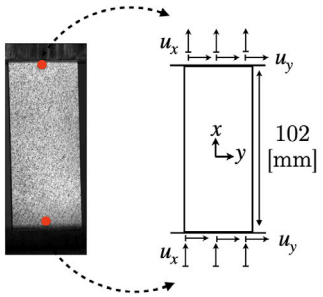

Fig. 23. Illustration of displacement boundary conditions for the finite element simulations. The red dot indicates the approximate location where the vertical and lateral displacements are extracted.

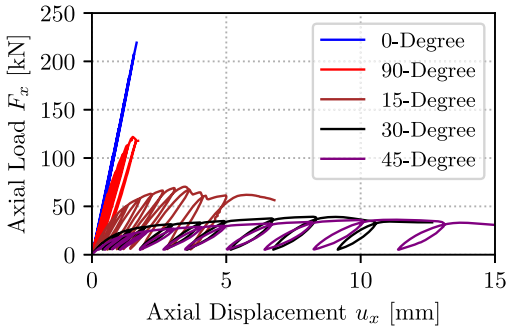

Fig. 24. Experimental results for the axial load–displacement curves for the different specimen angles. Note the load has been doubled for the 90° weft aligned sample for comparison.

lower grip. This is illustrated in Fig. 23. Both the vertical and lateral displacements extracted from the DIC-analysis were then mapped to the upper and lower surfaces of the FE-model.

4.1. Model behaviour and validation

Fig. 24 compares the resulting experimental force–displacement curves for each specimen angle. Similarly, Fig. 25 compares the load–displacement curve results from the FE-simulations up to the first load drop. Note that, in the case of the 90° specimen, the axial loads have been doubled (due to the narrower specimens) in order to allow for a more direct comparison. It is clear from the simulation results, that the model is able to capture trends that one would expect. The reinforcement oriented 0° and 90° samples show the stiffest response. The 15° and 30° samples show a gradual softening and increased response governed by the shear response, before the 45° sample shows the softest behaviour. However, it is also clear from Fig. 24 results that the 15° sample shows a far softer experimental response than that demonstrated by the model.

For further comparison, Fig. 26, Fig. 27 and Fig. 28 directly compare the experimental and simulation results for the 0°, 90° and 45° samples respectively. It is clear from the load–displacement curves that for these uniaxial loading modes, extracting the plasticity and damage parameters as described in Section 3.3, gives a high level of agreement between the predicted material response and the experimental results. Further, contour plots of the axial strain have been extracted at the locations indicated with a red star for each test. It should be noted that, as this is a macroscale model, when comparing the contour plots of the axial strain the model is not able to capture the localised strain concentrations. The main strain contour patterns seen using the DIC analysis on all test samples are highly influenced by the mesostructure of the material. The strains tend to localise in the resin pockets which are highly oriented and influenced by the orientation

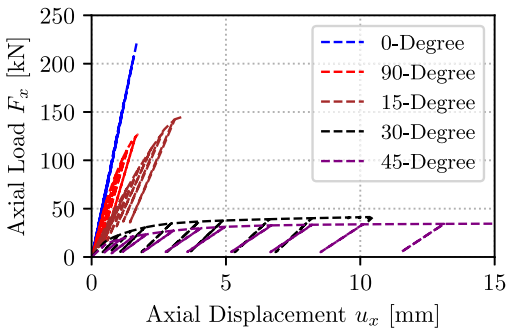

Fig. 25. Simulation results for the axial load–displacement curves for the different specimen angles. Note the load has been doubled for the 90° weft aligned sample for comparison. The experimental results are shown in (a) while the simulation results are shown in (b).

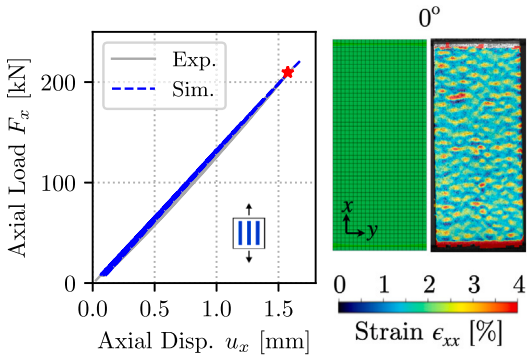

Fig. 26. Comparison of the experimental and simulation results for the 0° warp-aligned sample. The axial load–displacement curves are shown in the left image while the right image shows contour plots of the axial strain distributions taken at the location indicated with a red star.

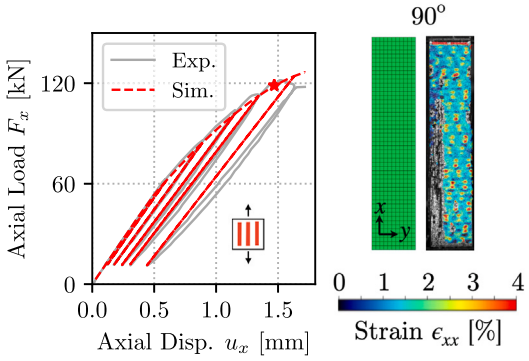

Fig. 27. Comparison of the experimental and simulation results for the 90° weft-aligned sample. The axial load–displacement curves are shown in the left image while the right image shows contour plots of the axial strain distributions taken at the location indicated with a red star. Note that to maintain consistency, the force values have been doubled.

of the reinforcement yarns. Macroscale models treat the material as a homogeneous solid and therefore do not capture these types of localised strain distributions.

Figs. 29 and 30 compare the load–displacement curves for the 15° and 30° specimens, respectively. In the case of the 30° off-axis sample, the simulation is again able to predict the material behaviour with good agreement. In the case of the 15° sample however, this is not the case. Although the initial elastic stiffness is predicted well, non-linear behaviours develop far sooner and more aggressively in the experimental test. One possible explanation could be the sample width

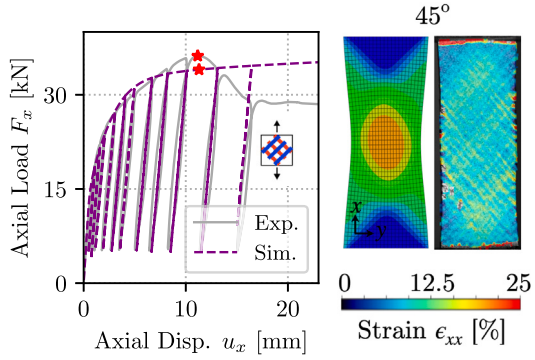

Fig. 28. Comparison of the experimental and simulation results for the 45° off-axis sample. The axial load–displacement curves are shown in the left image while the right image shows contour plots of the axial strain distributions taken at the location indicated with a red star.

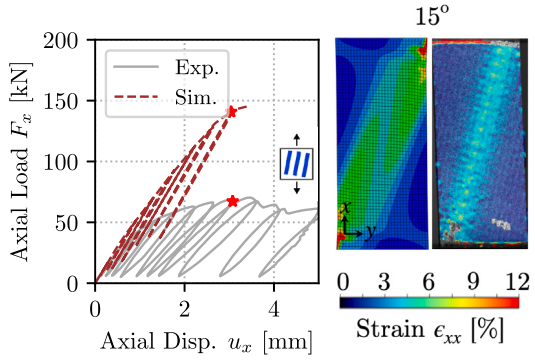

Fig. 29. Comparison of the experimental and simulation results for the 15° off-axis sample. The axial load–displacement curves are shown in the left image while the right image shows contour plots of the axial strain distributions taken at the location indicated with a red star.

and the angle. A small fraction of the reinforcement yarns will run unbroken (continuous reinforcement) from one grip to the other. This could lead to a far more shear-dominated deformation behaviour than what is predicted by the macroscale model. Regardless of the cause, it is however an indication that the model needs further development to account for these types of couplings between normal and shear loading. One option is then to switch from multiple yield surfaces and multiple damage surfaces to one anisotropic surface for each case.

From the contour plots of the axial strain in Fig. 29 and Fig. 30, it can be seen that the model does however clearly predict localised regions of high strain manifesting themselves as shear bands. Further, these shear bands are heavily tied to the orientation of the reinforcements. Again, as this is a macroscale model, the width and strain variations within this region are not well captured.

5. Conclusions and outlook

Composites with 3D-woven reinforcements have a number of promising characteristics related to both their manufacturability as well as their mechanical performance. The woven substructure however, can create a material with high levels of anisotropy. Further, the nature of the material leads to a variety of subscale mechanisms when loaded, which in turn manifest themselves as a non-linear mechanical response.

By cyclically loading material samples oriented at 0°, 90° and 45° relative to the material warp direction, it was shown that it is possible to differentiate between non-linear behaviour due to stiffness degradation (damage) and due to permanent strain development (plasticity). Notably, the multiple tests conducted per orientation angle

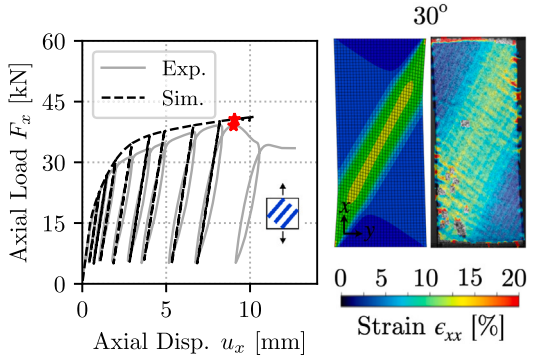

Fig. 30. Comparison of the experimental and simulation results for the 30° off-axis sample. The axial load–displacement curves are shown in the left image while the right image shows contour plots of the axial strain distributions taken at the location indicated with a red star.

showed high levels of consistency. Further, it was shown that different behaviours can be identified under warp, weft and shear dominated loading. The experimental data, which is made freely available, was then used to calibrate an anisotropic macroscale elastoplastic damage model developed by Oddy et al. [11]. The model showed good agreement with the experimental results. These cases however represent uniaxial loading modes.

For model validation, the material samples were also loaded in tension at other off-axis angles, specifically 15° and 30° relative to the warp direction. This imparts combined tensile and shear loading on the material sample. Again, the experimentally observed curves showed high consistency for the same loading angle. The corresponding simulation results showed that, while the model was able to predict the cyclic behaviour of the 30° with good agreement, the outcome of the 15° model results were less satisfactory. This likely indicates that the macroscale model still requires further development to account for the full impacts of multiaxial loading.

The future use of anisotropic damage and yield surfaces could provide one positive path forward. However, further testing is required in order to truly understand how the combination of tensile and shear load, either simultaneously or successively, impact the macroscale behaviour. Further experimental testing is also necessary for expanding the model to handle compressive loading and out-of-plane loading. One promising way to both reduce cost and circumvent challenges associated with more complex testing needs, is through the use of mesoscale models. This could mean that through the combination of experimental and virtual testing, it would be possible to obtain sufficient calibration data for more advanced macroscale models.

CRediT authorship contribution statement

Carolyn Oddy: Writing – review & editing, Writing – original draft, Visualization, Validation, Software, Resources, Methodology, Investigation, Funding acquisition, Data curation, Conceptualization. **Meng yi Song:** Writing – review & editing, Validation, Resources, Investigation, Data curation. **Christian Stewart:** Writing – review & editing, Validation, Resources, Investigation, Data curation. **Bassam El Said:** Writing – review & editing, Supervision, Funding acquisition. **Magnus Ekh:** Writing – review & editing, Supervision. **Stephen R. Hallett:** Writing – review & editing, Supervision, Funding acquisition. **Martin Fagerström:** Writing – review & editing, Supervision, Funding acquisition.

Declaration of competing interest

The authors declare that they have no known competing financial interests or personal relationships that could have appeared to influence the work reported in this paper.

Data availability

For each test sample orientation an excel file is provided containing the time and load signals. Associated DIC images are also provided at the same time intervals. Both are found at DOI:10.5281/zenodo.10980478 [31].

Acknowledgements

The project was financially supported by Chalmers' Area of Advance in Materials Science (2021–0037) as well as the Swedish Agency for Innovation Systems (2023-01565). The simulations were performed on resources at Chalmers Centre for Computational Science and Engineering (C3SE) provided by the Swedish National Infrastructure for Computing (SNIC). M. Fagerström also gratefully acknowledges the financial support through Vinnova's strategic innovation programme LIGHTer (2020-04526). The authors also gratefully acknowledge the support of the UK Engineering and Physical Sciences Research Council (EPSRC) through the grant "Hybrid Deterministic/Statistical Multi-scale Modelling Techniques for 3D Woven Composites" (EP/V050591/1). M. Song is supported through the Programme Grant 'Certification of Design: Reshaping the Testing Pyramid' (EP/S017038/1). C. Stewart is supported by the EPSRC through the CoSEM Centre for Doctoral Training grant no. EP/S021728/1.

References

[1] Stig F, Hallström S. Spatial modelling of 3D-woven textiles. Compos Struct 2012;94:1495–502.
[2] Lomov SV, Ivanov DS, Verpoest I, Zako M, Kurashiki T, Nakai H, et al. Meso-FE modelling of textile composites: Road map, data flow and algorithms. Compos Sci Technol 2007;67:1870–91.
[3] Green SD, Matveev MY, Long AC, Ivanov D, Hallett SR. Mechanical modelling of 3D woven composites considering realistic unit cell geometry. Compos Struct 2014;118:284–93.
[4] Lomov SV, Gusakov AV, Huysmans G, Prodromou A, Verpoest I. Finite element modelling of progressive damage in non-crimp 3D orthogonal weave and plain weave E-glass composites. Compos Sci Technol 2000;60:2083–95.
[5] Topalidis I, El Said B, Thompson AJ, Keulen J, Hallett SR. A numerical study of the effect of draping on the mechanical properties of 3D woven composites. In: ICCM international conferences on composite materials. 2019.
[6] Mazumder A, Zheng L, Jiao Y, Bullions T, Yu Y, Wang Y. Predictive modeling of 3D textile composites using realistic micromechanical representations. Composites B 2024;279(April):111441.
[7] Hirsekorn M, Marcin L, Godon T. Multi-scale modeling of the viscoelastic behavior of 3D woven composites. Composites A 2018;112:539–48.
[8] Shah SZ, Megat-Yusoff PS, Karuppanan S, Choudhry RS, Sajid Z. Multiscale damage modelling of 3D woven composites under static and impact loads. Composites A 2021;151(September):106659.
[9] El Said B, Daghia F, Ivanov D, Hallett SR. An iterative multiscale modelling approach for nonlinear analysis of 3D composites. Int J Solids Struct 2018;132–133:42–58.
[10] Hurmane A, Mavel A, Paulmier P, Laurin F. Combined experimental and modelling approaches for strength analysis of 3D woven composites: From elementary coupons to complex aeronautical structures. AerospaceLab J 2016;(12):1–11.
[11] Oddy C, Ekh M, Fagerström M. Macroscale modelling of 3D-woven composites: Elasto-plasticity and progressive damage. Int J Solids Struct 2022;250:111696.
[12] Ladeveze P, LeDantec E. Damage modelling of the elementary ply for laminated composites. Compos Sci Technol 1992;43(3):257–67.
[13] Zscheyge M, Böhm R, Hornig A, Gerritzen J, Gude M. Rate dependent non-linear mechanical behaviour of continuous fibre-reinforced thermoplastic composites – Experimental characterisation and viscoelastic-plastic damage modelling. Mater Des 2020;193:108827.
[14] Marcin L. Modélisation du comportement, de l'endommagement et de la rupture de matériaux composites à renforts tissés pour le dimensionnement robuste de structures (Ph.D. thesis), Université Bordeaux; 2010.
[15] Grassl P, Jirásek M. Damage-plastic model for concrete failure. Int J Solids Struct 2006;43:7166–96.
[16] Médeau V, Laurin F, Rannou J, Hurmane A, Quillent H, Lachaud F. Robust characterization of crack propagation in 3D woven composites and evidences of size dependency. Compos Struct 2019;225(April):111175.
[17] Ottosen NS, Ristinmaa M. The mechanics of constitutive modeling. Elsevier Ltd; 2005.
[18] Médeau V. Rupture des composites tissés 3D: De la caractérisation expérimentale à la simulation robuste des effets d'échelle (Ph.D. thesis), Université De Toulouse; 2019.
[19] Miehe C, Welschinger F, Hofacker M. Thermodynamically consistent phase-field models of fracture: Variational principles and multi-field FE implementations. Internat J Numer Methods Engrg 2010;83:1273–311.
[20] Pijaudier-Cabot G, Bazant ZP. Nonlocal damage theory. J Eng Mech 1987;113:1512–33.
[21] Peerlings RHJ, de Borst R, Brekelmans WAM, de Vree JHP. Gradient enhanced damage for quasi-brittle materials. Internat J Numer Methods Engrg 1996;39:3391–403.
[22] Datenblatt: HexFlow RTM6. 2016.
[23] Tarnopol'skii YM, Kinics T. Static test methods for composites. Van Nostrand Reinhold Company; 1981.
[24] Sun CT, Berreth SP. A new end tab design for off-axis tension test of composite materials. J Compos Mater 1988;22(8):766–79.
[25] Adams DF, Carlsson LA, Pipes RB. Experimental characterization od advanced composite materials. 3rd ed.. CRC Press; 2003, p. 258.
[26] LaVision. Strain master, system components and accessories. https://www.lavision.de/en/products/strainmaster.
[27] Butterworth S. On the theory of filter amplifiers. Exp Wirel Wirel Eng 1930;(October):536–41.
[28] Oddy C. Macroscale modelling of 3D-woven composites: Inelasticity, progressive damage and final failure (Ph.D. thesis), Chalmers University of Technology; 2022.
[29] Oddy C, Song M, Stewart C, El Said B, Hallett SR, Fagerström M. On and off-axis cyclic behaviour of 3D-woven composites: Experimental testing and macroscale modelling. In: 9th ECCOMAS thematic conference on the mechanical response of composites. Trapani, Sicily; 2023.
[30] Simo J, Hughes T. Computational inelasticity, Vol. 7. Springer; 1998.
[31] Oddy C, Song M, Stewart C, El Said B, Ekh M, Fagerström M, et al. DIC images and data of in-plane cyclic testing of a 3D-woven layer-to-layer angle interlock composite [data set], Zenodo, http://dx.doi.org/10.5281/zenodo.10980478.